APL Materials

Engineering the oxygen coordination in digital superlattices

Cite as: APL Mater. **5**, 126101 (2017); https://doi.org/10.1063/1.5007663
Submitted: 02 October 2017 • Accepted: 09 November 2017 • Published Online: 01 December 2017

Seyoung Cook, Tassie K. Andersen, Hawoong Hong, et al.

Engineering the oxygen coordination in digital superlattices

Seyoung Cook,[1,2] Tassie K. Andersen,[1,2] Hawoong Hong,[3]
Richard A. Rosenberg,[3] Laurence D. Marks,[2] and Dillon D. Fong[1]
[1]*Materials Science Division, Argonne National Laboratory, Argonne, Illinois 60439, USA*
[2]*Department of Materials Science, Northwestern University, Evanston, Illinois 60202, USA*
[3]*X-Ray Science Division, Argonne National Laboratory, Argonne, Illinois 60439, USA*

(Received 2 October 2017; accepted 9 November 2017; published online 1 December 2017)

The oxygen sublattice in complex oxides is typically composed of corner-shared polyhedra, with transition metals at their centers. The electronic and chemical properties of the oxide depend on the type and geometric arrangement of these polyhedra, which can be controlled through epitaxial synthesis. Here, we use oxide molecular beam epitaxy to create $SrCoO_x$:$SrTiO_3$ superlattices with tunable oxygen coordination environments and sublattice geometries. Using synchrotron X-ray scattering in combination with soft X-ray spectroscopy, we find that the chemical state of Co can be varied with the polyhedral arrangement, with higher Co oxidation states increasing the valence band maximum. This work demonstrates a new strategy for engineering unique electronic structures in the transition metal oxides using short-period superlattices. https://doi.org/10.1063/1.5007663

The wide range of physical properties in perovskite-based transition metal oxides with the ABO_3 structural framework stems from the interplay of the lattice, charge, and orbital degrees of freedom.[1,2] One of the most direct ways to engineer functional properties in oxides is to modify the oxygen coordination environment of the B-site cation by geometric design, in which the structures of dissimilar oxides are coupled.[3–7] In the absence of oxygen vacancies, structural coupling at symmetry-mismatched interfaces can trigger or suppress octahedral rotations and deformations, for instance, to finely tune magnetic properties[8–10] and stabilize unusual coexisting properties.[11,12] However, in the case of oxides with multivalent B-site cations that readily form oxygen vacancies, lattice mismatch can change the degree of oxygen nonstoichiometry.[13,14] The variable oxygen stoichiometry allows different electronic and magnetic ground states to be stabilized[14–17] and enables high oxygen redox activity and/or facile oxygen anion diffusion for improved catalytic activities.[18,19]

One notable oxide in this regard is strontium cobaltite, $SrCoO_x$, wherein the Co oxidation state can change from +3 to +4 as the oxygen content x changes from 2.5 to 3, resulting in highly contrasting electronic and magnetic ground states. The reduced end member, brownmillerite $SrCoO_{2.5}$ (BM-SCO), is an antiferromagnetic insulator with a bandgap of 2.12 eV,[20] while the oxidized cubic perovskite $SrCoO_{3-\delta}$ (P-SCO) is a ferromagnetic metal.[21,22] The orthorhombic BM-SCO unit cell can be represented by a pseudotetragonal structure with a_t = 3.905 Å, taken as an average of the in-plane orthorhombic lattice parameters a_o = 5.5739(2) Å, b_o = 5.4697(2) Å, and c_t = 15.7450(5) Å.[23–25] This structure consists of four alternating layers of corner-shared CoO_4 tetrahedra and CoO_6 octahedra, as shown in Fig. 1(a). On the other hand, $SrTiO_3$ (STO) is a cubic perovskite and non-magnetic insulator with a bandgap of 3.2 eV.[26] It is entirely composed of TiO_6 octahedra with a lattice parameter of a_c = 3.905 Å, also shown in Fig. 1(a), and offers 1% compressive and tensile strains with respect to the individual a_o and b_o lattice parameters of BM-SCO.[27] Here, the Ti cation strongly prefers the +4 oxidation state regardless of the environmental conditions.

With the many recent advances in oxide thin film synthesis, we are now able to modulate the B-site sublattice at the atomic level. It should then be possible to manipulate and stabilize the total oxygen vacancy concentration and overall Co oxidation state, not simply by varying between the $SrCoO_{2.5}$

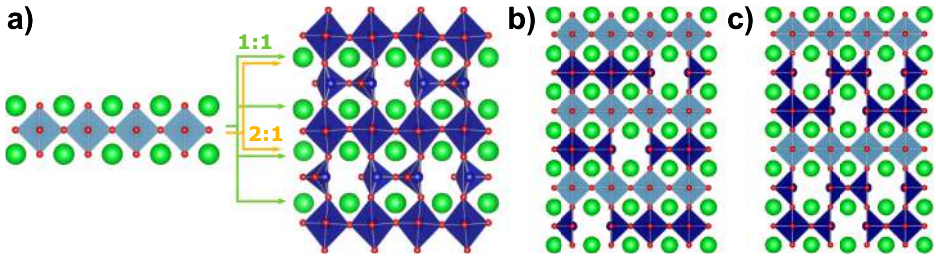

FIG. 1. Schematic illustrations of the $SrCoO_x$-$SrTiO_3$ structures. Sr atoms are shown in green, oxygen atoms are red, and the Ti and Co atoms are centered within the gray-blue and dark blue polyhedra, respectively. (a) Illustration of the $SrTiO_3$ (left) and $SrCoO_{2.5}$ (right) unit cells, with arrows showing how $SrTiO_3$ is inserted within $SrCoO_{2.5}$ to make the 2:1 and 1:1 superlattices of $SrCoO_x$ and $SrTiO_3$. [(b) and (c)] Illustrations of the $(SrCoO_x)_1 : (SrTiO_3)_1$ (b) and $(SrCoO_x)_2 : (SrTiO_3)_1$ (c) superlattices.

and $SrCoO_3$ phases, but through the strategic design and *placement* of Co and Ti ions throughout a digital superlattice. In this work, we create and investigate the oxygen coordination environment of Co and the electronic structures of $Sr(Co,Ti)O_x$ artificial crystals, whereby we interweave the $SrCoO_{2.5}$ lattice with a single layer of $SrTiO_3$, as shown schematically in Fig. 1(a). Specifically, we examine $(SrCoO_x)_n : (SrTiO_3)_1$ ($n = 1, 2$) superlattices (SLs), as illustrated in Figs. 1(b) and 1(c) for the 1:1 SL and the 2:1 SL, respectively. The results are compared with a 50:50 solid solution of $Sr(Co,Ti)O_x$. We find that the spatial order of Co and Ti cations determines the resulting oxidation state, with the 1:1 superlattice resulting in $Co^{3.5+}$ and the 2:1 superlattice and the 50:50 alloy both resulting in $Co^{3.25+}$. This study demonstrates a new strategy for tuning the oxidation state of a multivalent B-site cation through the design and synthesis of short-period superlattices.

The superlattices were synthesized by ozone-assisted molecular beam epitaxy (MBE) in a chamber located at Sector 33ID-E of the Advanced Photon Source (APS). All films were deposited on conducting 0.05 wt. % (0.1 at. %) Nb-doped $SrTiO_3$ (0 0 1) substrates (to prevent charging in subsequent soft X-ray measurements), prepared with TiO_2-terminated surfaces using the procedure described in Ref. 28. After performing growths in a range of conditions, from 550 °C to 750 °C and in different oxidizing environments, we found that the optimal conditions for synthesis were at 610 °C in 1×10^{-6} Torr ozone, which resulted in sharp heterointerfaces, good crystallinity, and minimal secondary phase formation. Consequently, all of the results presented are from films grown under these conditions after cooling to room temperature in the same ozone pressure at ~10 °C/min to prevent oxygen loss. The thicknesses of the individual $SrTiO_3$ and $SrCoO_{2.5}$ layers were calibrated immediately prior to superlattice deposition. Fifteen repeat units were grown by shuttered deposition for the superlattices, corresponding to 30 monolayers or ~11 nm for the $n = 1$ superlattice (1:1 SL) and 45 monolayers or ~17 nm for the $n = 2$ superlattice (2:1 SL). For comparison, we also grew a 11-nm-thick alloy of $Sr(Co_{0.5},Ti_{0.5})O_x$ (50:50 alloy), where Co and Ti were co-deposited, and a 6-nm-thick BM-SCO thin film. All subsequent measurements were performed at room temperature, as detailed in the experimental section (see the supplementary material).

Figure 2 shows the scattered intensities measured along the specular 00*L* rod for the BM-SCO and the SCO-STO thin films taken with 8-keV X-rays immediately after cooling the thin films to room temperature. Superlattice peaks are clearly observed for the 1:1 and 2:1 SLs despite the similarity in the Co and Ti atomic numbers, indicating the presence of fairly well-ordered interfaces. Half-order peaks characteristic of the brownmillerite structure are observed for the BM-SCO thin film, while much weaker half-order peaks are seen for the 1:1 SL. The weaker intensities indicate that the 1:1 SL adopts a more perovskite-like structure in which the SrO layers separating the Co and Ti layers are spaced more evenly apart compared to the brownmillerite structure, in which the SrO interlayer distances separating the octahedral CoO_6 and tetrahedral CoO_4 layers differ by 0.87 Å.[24] The 2:1 SL shows the expected 1/3-order superlattice peaks, while the 50:50 alloy shows an absence of any superlattice peaks. In the case of the 1:1 SL and the 50:50 alloy, a small peak corresponding to CoO (2 0 0) is observed at $L = 1.8$ reciprocal lattice units (r.l.u.), together with precipitates in atomic force microscopy (AFM) images (Fig. S1 of the supplementary material). This indicates the presence

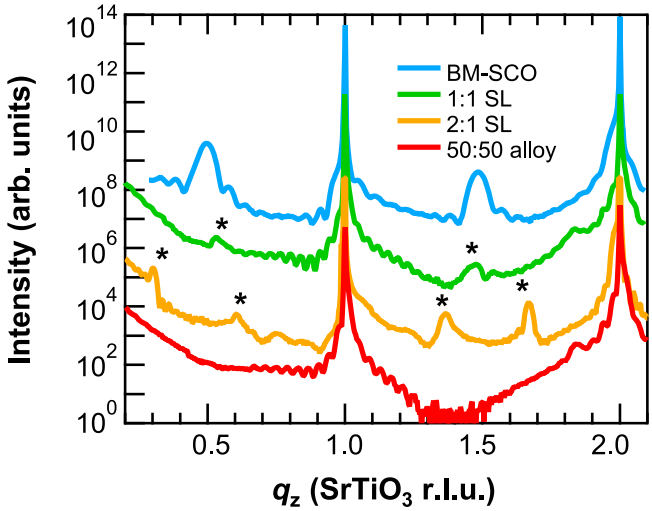

FIG. 2. Scattered intensities along the 00*L* crystal truncation rod for the brownmillerite $SrCoO_{2.5}$ (BM-SCO) film, cobaltite-titanate superlattices, and thin film alloy. The superlattice peaks are marked by *.

of a small amount of CoO in the films (<1.4 vol. %), which, as discussed below, was investigated in more detail using soft X-ray spectroscopy performed at Sector 4ID-C of the APS.

To determine the oxygen coordination environment of Ti in the cobaltite-titanate films, results from Ti 2*p* X-ray photoelectron spectroscopy (XPS) and Ti *L*-edge X-ray absorption spectroscopy (XAS) were compared with those from a bare 0.05 wt. % (0.1 at. %) Nb-doped $SrTiO_3$ substrate (Nb:STO). The Ti 2*p* core-level XPS spectra of the cobaltite-titanate films were fit using the same Gaussian-Lorentzian peak shapes used for the Nb:STO Ti 2*p* XPS spectrum, as shown in Fig. 3(a). The good agreement of the fits indicates negligible Ti^{3+} states within the 3.7 nm 95% probe depth.[29] This observation is consistent with the Ti $L_{3,2}$-edge X-ray absorption spectra of the cobaltite-titanate films shown in Fig. 3(b), which are characteristic of Ti^{4+} subject to an octahedral crystal field.[30] A close comparison of the Ti $L_{3,2}$-edge line shapes shows that the cobaltite-titanate films contain extra spectral weight between the t_{2g} and e_g manifolds compared to the Nb:STO Ti *L*-edge spectrum (see Fig. S2 of the supplementary material). We attribute this small deviation from the reference Ti^{4+} O_6

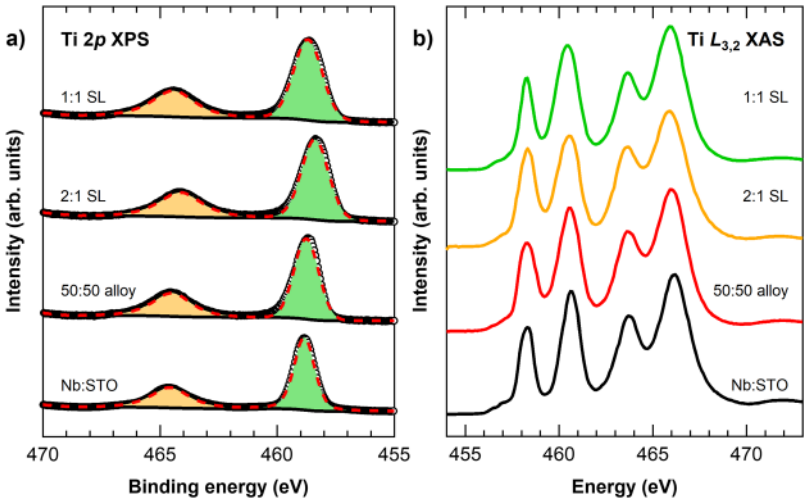

FIG. 3. Ti 2*p* core-level spectra showing persistent $Ti^{4+}O_6$ octahedra in the cobaltite-titanate thin films. (a) Ti 2*p* core-level photoelectron spectra of the thin films compared with those of a bare 0.05 wt. % Nb-doped $SrTiO_3$ substrate (Nb:STO). (b) The corresponding Ti $L_{3,2}$-edge X-ray absorption spectra.

spectrum to disorder-induced peak broadening caused by the presence of Ti–O–Co bonds in addition to the Ti–O–Ti bonds. No extra intensity was observed at ~457 eV for any of these films, which would otherwise appear in the presence of Ti^{3+}.[31,32] We thus confirm that virtually all Ti ions in the cobaltite-titanate films maintain the Ti^{4+} oxidation state within an octahedral coordination environment, which in turn indicates that oxygen vacancies in the films are confined to the first coordination shell of Co.

Given the persistent $Ti^{4+}O_6$ octahedra and the corresponding localization of oxygen vacancies around Co, XAS was performed at the Co $L_{3,2}$ edge to probe simultaneously the oxygen coordination environment and oxidation state of the Co ions. After first accounting for the small CoO contribution (see Fig. S3 of the supplementary material), each spectrum was assigned to mixed Co^{3+}/Co^{4+} contribution intrinsic to the respective cobaltite-titanate film arising from a mixture of square pyramidal CoO_5 and octahedral CoO_6 units. There exist clear chemical shifts of the sharp L_3 peak corresponding to the Co^{3+}/Co^{4+} contribution, as shown in the inset of Fig. 4(a). Comparison with reference spectra

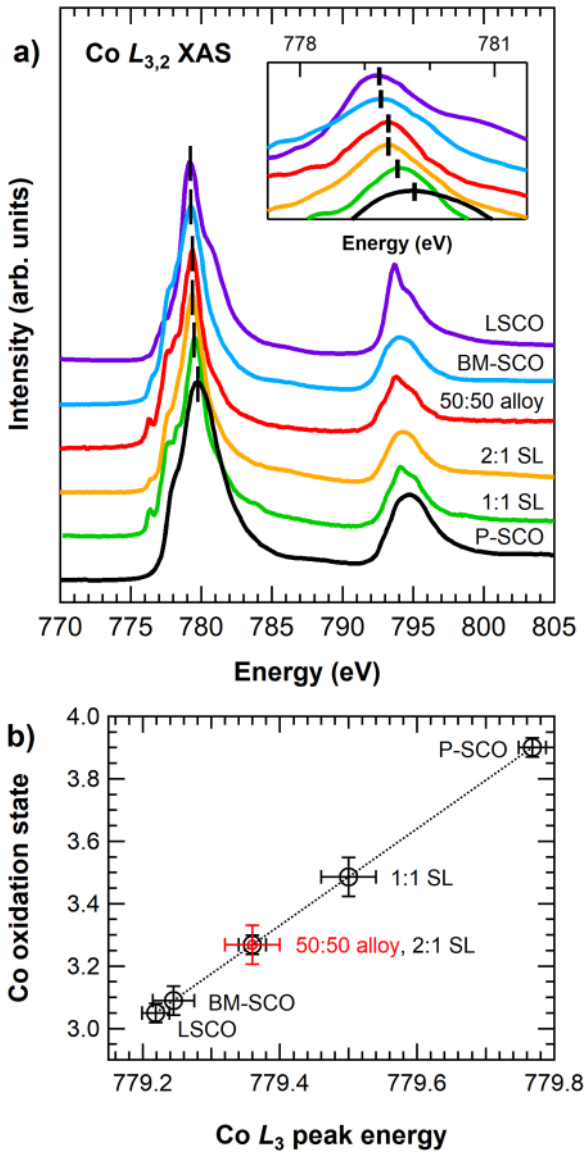

FIG. 4. Results on the chemical properties of Co in the thin film samples and reference materials. (a) Co $L_{3,2}$ X-ray absorption spectra of the cobaltite-titanate films compared with those of brownmillerite $SrCoO_{2.5}$ (BM-SCO), $La_{0.95}Sr_{0.05}CoO_3$ (LSCO), and perovskite $SrCoO_{2.9}$ (P-SCO). (b) Co oxidation state determined from the Co L_3 peak energy. The dotted line serves as a visual guide to the trend.

of $La_{0.95}Sr_{0.05}CoO_3$ (LSCO), with a nominal Co oxidation state of +3.05, and perovskite $SrCoO_{2.9}$ (P-SCO), with a Co oxidation state of +3.9 taken from Ref. 13, reveals a varying Co oxidation state that is dependent on the geometric arrangement of Co and Ti in the cobaltite-titanate thin films, as summarized in Fig. 4(b). The 1:1 SL, containing the same Co/Ti ratio as the 50:50 alloy, exhibits a Co oxidation state of +3.5. Interestingly, the random alloy exhibits a lower Co oxidation state of +3.25. However, the 2:1 SL, with twice the Co/Ti ratio as the 50:50 alloy, also displays a Co oxidation state of +3.25.

We calculated the average oxygen coordination of the Co atoms and the corresponding oxygen stoichiometry in the cobaltite-titanate thin films by considering the Co oxidation state, which is effectively a measure of the Co valence, as the sum of the nominal bond valences of the three types of bonds surrounding the Co atom, Co–O–Co, Co–V_O–Co, and Co–O–Ti, where V_O denotes a vacant oxygen site (see Table S1 of the supplementary material). This reveals stoichiometries of $(SrCoO_{2.76})_1 : (SrTiO_3)_1$ and $(SrCoO_{2.64})_2 : (SrTiO_3)_1$ for the 1:1 SL and the 2:1 SL, respectively, with corresponding 50:50 and 75:25 ratios of square pyramidal CoO_5 and octahedral CoO_6 units. This is attributable to the persistent octahedral $Ti^{4+}O_6$ units that suppress oxygen vacancy formation around nearest-neighbor Co atoms by the formation of Co–O–Ti bonds. Having fewer consecutive CoO_x layers in the 1:1 SL versus the 2:1 SL suppresses oxygen vacancy formation more and thus stabilizes a higher Co oxidation state. In the case of the 50:50 alloy, the stoichiometry corresponds to $Sr(Co_{0.5},Ti_{0.5})O_{2.82}$, with the same 25:75 ratio of square pyramidal CoO_5 to octahedral CoO_6 found in the 2:1 SL. The random arrangement of Co and Ti in the 50:50 alloy promotes oxygen vacancy formation and stabilizes a lower Co oxidation state compared to the short-period layered arrangement in the 1:1 SL.

We also note that while ferromagnetic order has been observed in $SrCoO_{2.75}$ thin films with $Co^{3.5+}$,[14] X-ray magnetic circular dichroism (XMCD) measurements performed at 40 K in a 0.5 T field did not provide conclusive evidence for such behavior in any of the superlattices or the 50:50 alloy (see Fig. S4 of the supplementary material). While this may be due to the proximity of Co and Ti cations, further studies on $(SrCoO_x)_n : (SrTiO_3)_1$ superlattices will be necessary.

To investigate how the electronic structure of the cobaltite-titanate films evolves from the characteristic properties of STO and BM-SCO, we performed resonant photoemission spectroscopy (RESPES) at the Ti 2*p*-3*d* and Co 2*p*-3*d* thresholds to distinguish the occupied element-projected and orbital 3*d* partial density of states in the valence band. Figure 5(b) shows the Ti 2*p*-3*d* valence band spectra for the 1:1 SL obtained with photon energies (A)–(E) marked in Fig. 5(a). Photon energies corresponding to similar features in the Ti $L_{3,2}$ XAS spectrum were chosen for the Ti 2*p*-3*d* valence band spectra of the 2:1 SL and 50:50 alloy, shown in Figs. 5(c) and 5(d), respectively. Comparison of the off-resonance spectrum (A) with on-resonance spectra (B)–(E) indicates that the resonant enhancement of the valence band spectra is limited to the states around 4.4 eV and 6.4 eV binding energies, which contain contributions from the non-bonding and bonding Ti 3*d*-O 2*p* states in $SrTiO_3$, respectively.[33,34] The states peaked at 2.5 eV at the top of the valence band show negligible enhancement in intensity, which confirms that the top of the valence band is predominantly composed of Co 3*d*-O 2*p* states. This is consistent with the observed minimal enhancement of states in the gap at the Ti 2*p*-3*d* resonance.

Figure 5(f) shows the Co 2*p*-3*d* valence band spectra for the 1:1 SL obtained with the photon energies (A)–(E) marked in Fig. 5(e). Photon energies corresponding to similar features in the Co $L_{3,2}$ XAS spectrum were chosen for the Co 2*p*-3*d* valence band RESPES of the 2:1 SL and 50:50 alloy, shown in Figs. 5(g) and 5(h), respectively. In contrast to the Ti 2*p*-3*d* valence band spectra, resonant enhancement in the intensity is observed throughout the entirety of the valence band region, confirming the presence of Co 3*d* states that extend into the bandgap region of $SrTiO_3$. In addition, a clear Fermi-edge step is observed at strong Co 2*p*-3*d* resonance (D), indicating small contributions of defect states with significant Co 3*d* character within the gap. The Fermi levels of the cobaltite-titanate thin films were determined by fitting the Fermi-edge steps apparent at strong Co 2*p*-3*d* resonance (dashed lines). This allowed the determination of the valence band maximum (VBM) of each film by extrapolating the linear portion of the valence band edge to the background from the off-resonance valence band XPS spectra taken with photon energies of 772 eV and 1000 eV for the cobaltite-titanate thin films and the Nb:STO sample, respectively, as shown in Fig. 6. The valence band

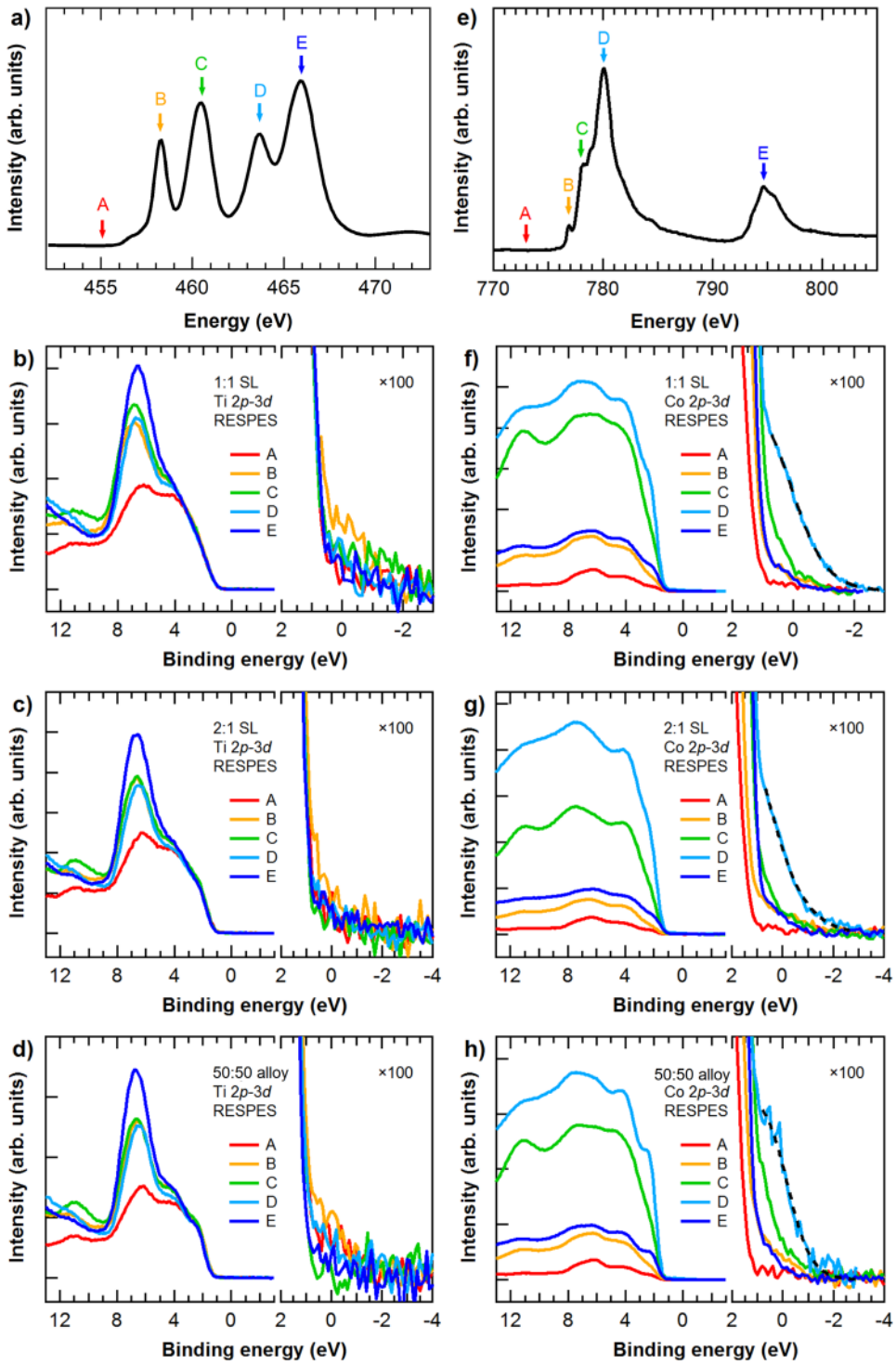

FIG. 5. Resonant photoemission spectra measured in the valence band region at the Ti 2*p*-3*d* and Co 2*p*-3*d* absorption thresholds. (a) Ti $L_{3,2}$ XAS spectrum of the 1:1 SL. [(b)–(d)] RESPES spectra at Ti 2*p*-3*d* resonance plotted in wide region (left) and in enlarged scale (×100) near the Fermi level ($E_F = 0$ eV) (right). The labels (A)–(E) correspond to excitation photon energies as marked in (a) for the 1:1 SL and to energies chosen at similar features in the Ti $L_{3,2}$ XAS spectra for the 2:1 SL and the 50:50 alloy. (e) Co $L_{3,2}$ XAS spectrum of the 1:1 SL including the CoO component. [(f)–(h)] RESPES spectra at Co 2*p*-3*d* resonance for the cobaltite-titanate thin films taken in similar fashion as the Ti 2*p*-3*d* valence band RESPES spectra. The dashed lines are the fitting curves of the RESPES spectra at strong Co 2*p*-3*d* resonance (D), showing a clear Fermi-edge step in each film.

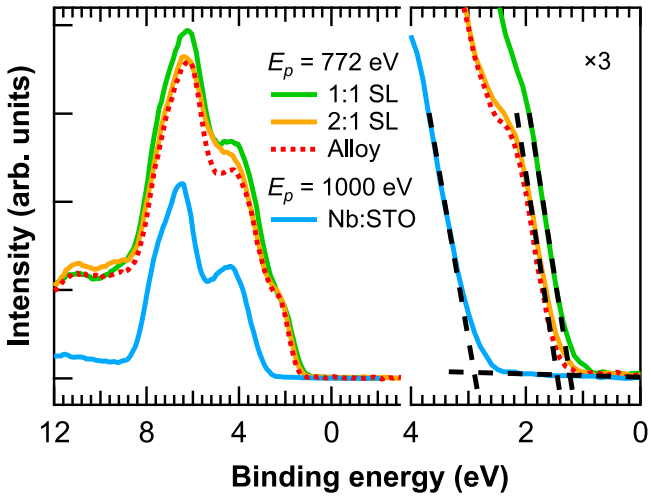

FIG. 6. X-ray photoelectron spectra of the valence band region. The valence band maxima of the cobaltite-titanate thin films are compared with those from the *n*-type 0.05 wt. % Nb-doped $SrTiO_3$ sample.

maxima are found at binding energies of 1.2 eV for the 1:1 SL and 1.4 eV for the 2:1 SL and the 50:50 alloy, showing that the VBM increases with the average Co oxidation state in the cobaltite-titanate films.

As an internal check, we also considered the valence band spectrum of the Nb:STO substrate, taken with 1000 eV photon energy, which was aligned in the binding energy scale using the Sr 4*s* and O 2*s* core-level peaks at 19.3 eV and 21.8 eV binding energies, respectively (see Fig. S5 of the supplementary material). This procedure yields a VBM of 2.9 eV for the Nb:STO that is located just below the conduction band of $SrTiO_3$, as shown in Fig. 6, in line with the value for *n*-type $SrTiO_3$ reported by Chambers and co-workers.[35] Furthermore, the alignment of the spectral features at 4.4 eV and 6.4 eV binding energies corresponding to the non-bonding and bonding Ti 3*d*-O 2*p* states of the Nb:STO with those of the cobaltite-titanate films indicates that the Fermi levels in the cobaltite-titanate films coincide with the Fermi level in Nb:STO. This is consistent with our picture of a variable Co oxidation state as the Co valence derived from the corresponding oxygen stoichiometry rather than electronic holes combined with $SrTi^{4+}_{1-x}Co^{3+}_{x}O_{3-x/2}$, which would lower the Fermi level.

In summary, we find that the oxygen vacancy concentration, the Co oxidation state, and the resulting valence band maximum of the material can be tuned geometrically, i.e., through atomic-level manipulation of the Co and Ti nearest neighbors throughout an oxide crystal. Furthermore, we demonstrate control over the spatial arrangement of oxygen vacancies in an oxide crystal, which we and others have shown to be useful in modulating electronic, magnetic, and catalytic behaviors.[36–39] By employing different arrangements of CoO_x and TiO_2 layers under the same epitaxial strain and growth conditions, the Co oxidation state can be raised from the nominal +3 found in brownmillerite $SrCoO_{2.5}$ to +3.25 and +3.5 in $(SrCoO_{2.64})_2 : (SrTiO_3)_1$ and $(SrCoO_{2.76})_1 : (SrTiO_3)_1$ superlattices, respectively. The results illustrate how interface engineering can be combined with defect control to achieve novel properties in complex oxides.

See supplementary material for the details of the experimental methods, AFM micrographs, and additional information regarding the Co *L*-edge XAS spectra, determination of the oxygen stoichiometries, XMCD results, and the valence band XPS spectra.

S.C., T.K.A., and D.D.F. were supported by the U.S. Department of Energy, Office of Science, Materials Sciences and Engineering Division. Use of the Advanced Photon Source was supported by the U.S. Department of Energy, Office of Science, Office of Basic Energy Sciences, under Contract No. DE-AC02-06CH11357. We thank J. W. Freeland and J. F. Mitchell for providing the LSCO and P-SCO reference spectra.

[1] Y. Tokura and N. Nagaosa, Science **288**, 462 (2000).
[2] E. Dagotto, Science **309**, 257 (2005).
[3] D. G. Schlom, L.-Q. Chen, C.-B. Eom, K. M. Rabe, S. K. Streiffer, and J.-M. Triscone, Annu. Rev. Mater. Res. **37**, 589 (2007).
[4] P. Zubko, S. Gariglio, M. Gabay, P. Ghosez, and J.-M. Triscone, Annu. Rev. Condens. Matter Phys. **2**, 141 (2011).
[5] H. Y. Hwang, Y. Iwasa, M. Kawasaki, B. Keimer, N. Nagaosa, and Y. Tokura, Nat. Mater. **11**, 103 (2012).
[6] J. M. Rondinelli, S. J. May, and J. W. Freeland, MRS Bull. **37**, 261–270 (2012).
[7] A. Bhattacharya and S. J. May, Annu. Rev. Mater. Res. **44**, 65 (2014).
[8] Z. Liao, M. Huijben, Z. Zhong, N. Gauquelin, S. Macke, R. J. Green, S. Van Aert, J. Verbeeck, G. Van Tendeloo, K. Held, G. A. Sawatzky, G. Koster, and G. Rijnders, Nat. Mater. **15**, 425 (2016).
[9] D. Kan, R. Aso, R. Sato, M. Haruta, H. Kurata, and Y. Shimakawa, Nat. Mater. **15**, 432 (2016).
[10] L. Qiao, J. H. Jang, D. J. Singh, Z. Gai, H. Xiao, A. Mehta, R. K. Vasudevan, A. Tselev, Z. Feng, H. Zhou, S. Li, W. Prellier, X. Zu, Z. Liu, A. Borisevich, A. P. Baddorf, and M. D. Biegalski, Nano Lett. **15**, 4677 (2015).
[11] M. J. Pitcher, P. Mandal, M. S. Dyer, J. Alaria, P. Borisov, H. Niu, J. B. Claridge, and M. J. Rosseinsky, Science **347**, 420 (2015).
[12] T. H. Kim, D. Puggioni, Y. Yuan, L. Xie, H. Zhou, N. Campbell, P. J. Ryan, Y. Choi, J.-W. Kim, J. R. Patzner, S. Ryu, J. P. Podkaminer, J. Irwin, Y. Ma, C. J. Fennie, M. S. Rzchowski, X. Q. Pan, V. Gopalan, J. M. Rondinelli, and C. B. Eom, Nature **533**, 68 (2016).
[13] H. Jeen, W. S. Choi, M. D. Biegalski, C. M. Folkman, I.-C. Tung, D. D. Fong, J. W. Freeland, D. Shin, H. Ohta, M. F. Chisholm, and H. N. Lee, Nat. Mater. **12**, 1057 (2013).
[14] J. R. Petrie, C. Mitra, H. Jeen, W. S. Choi, T. L. Meyer, F. A. Reboredo, J. W. Freeland, G. Eres, and H. N. Lee, Adv. Funct. Mater. **26**, 1564 (2016).
[15] Y. Tsujimoto, C. Tassel, N. Hayashi, T. Watanabe, H. Kageyama, K. Yoshimura, M. Takano, M. Ceretti, C. Ritter, and W. Paulus, Nature **450**, 1062 (2007).
[16] J. Young and J. M. Rondinelli, Phys. Rev. B **92**, 174111 (2015).
[17] Q. Lu and B. Yildiz, Nano Lett. **16**, 1186 (2016).
[18] H. Jeen, Z. Bi, W. S. Choi, M. F. Chisholm, C. A. Bridges, M. P. Paranthaman, and H. N. Lee, Adv. Mater. **25**, 6459 (2013).
[19] J. R. Petrie, H. Jeen, S. C. Barron, T. L. Meyer, and H. N. Lee, J. Am. Chem. Soc. **138**, 7252 (2016).
[20] N. Lu, P. Zhang, Q. Zhang, R. Qiao, Q. He, H.-B. Li, Y. Wang, J. Guo, D. Zhang, Z. Duan, Z. Li, M. Wang, S. Yang, M. Yan, E. Arenholz, S. Zhou, W. Yang, L. Gu, C.-W. Nan, J. Wu, Y. Tokura, and P. Yu, Nature **546**, 124 (2017).
[21] Y. Long, Y. Kaneko, S. Ishiwata, Y. Taguchi, and Y. Tokura, J. Phys.: Condens. Matter **23**, 245601 (2011).
[22] T. Takeda, Y. Yamaguchi, and H. Watanabe, J. Phys. Soc. Jpn. **33**, 970 (1972).
[23] H. Jeen, W. S. Choi, J. W. Freeland, H. Ohta, C. U. Jung, and H. N. Lee, Adv. Mater. **25**, 3651 (2013).
[24] A. Muñoz, C. de la Calle, J. A. Alonso, P. M. Botta, V. Pardo, D. Baldomir, and J. Rivas, Phys. Rev. B **78**, 054404 (2008).
[25] A. Nemudry, P. Rudolf, and R. Schöllhorn, Chem. Mater. **8**, 2232 (1996).
[26] M. Capizzi and A. Frova, Phys. Rev. Lett. **25**, 1298 (1970).
[27] T. L. Meyer, H. Jeen, X. Gao, J. R. Petrie, M. F. Chisholm, and H. N. Lee, Adv. Electron. Mater. **2**, 1500201 (2016).
[28] G. Koster, B. L. Kropman, G. J. H. M. Rijnders, D. H. A. Blank, and H. Rogalla, Appl. Phys. Lett. **73**, 2920 (1998).
[29] $3\lambda \sin\theta$, where λ is the photoelectron inelastic mean free path and θ is the emission angle measured from the sample surface, in this case for 1000 eV photon energy with $\theta = 80°$.
[30] F. M. F. de Groot, J. C. Fuggle, B. T. Thole, and G. A. Sawatzky, Phys. Rev. B **41**, 928 (1990).
[31] M. Abbate, F. M. F. de Groot, J. C. Fuggle, A. Fujimori, Y. Tokura, Y. Fujishima, O. Strebel, M. Domke, G. Kaindl, J. van Elp, B. T. Thole, G. A. Sawatzky, M. Sacchi, and N. Tsuda, Phys. Rev. B **44**, 5419 (1991).
[32] A. Ohtomo, D. A. Muller, J. L. Grazul, and H. Y. Hwang, Nature **419**, 378 (2002).
[33] Y. Adachi, S. Kohiki, K. Wagatsuma, and M. Oku, J. Appl. Phys. **84**, 2123 (1998).
[34] S. Kohiki, M. Arai, H. Yoshikawa, S. Fukushima, M. Oku, and Y. Waseda, Phys. Rev. B **62**, 7964 (2000).
[35] S. Chambers, T. Droubay, T. Kaspar, M. Gutowski, and M. van Schilfgaarde, Surf. Sci. **554**, 81 (2004).
[36] R. Mishra, Y.-M. Kim, J. Salafranca, S. K. Kim, S. H. Chang, A. Bhattacharya, D. D. Fong, S. J. Pennycook, S. T. Pantelides, and A. Y. Borisevich, Nano Lett. **14**, 2694 (2014).
[37] J. Young, E. J. Moon, D. Mukherjee, G. Stone, V. Gopalan, N. Alem, S. J. May, and J. M. Rondinelli, J. Am. Chem. Soc. **139**, 2833 (2017).
[38] H. A. Tahini, X. Tan, U. Schwingenschlögl, and S. C. Smith, ACS Catal. **6**, 5565 (2016).
[39] R. F. Berger, D. P. Broberg, and J. B. Neaton, APL Mater. **2**, 046101 (2014).